Homogenizing Morphology and Composition of Methylammonium-Free Wide-Bandgap Perovskite for Efficient and Stable Tandem Solar Cells

Peer-reviewed author version

Lian, Xinxin; Xu, Ye; Fu, Wei; Meng, Rui; Ma, Quanxing; Xu , Chunyu; Luo, Ming; Hu, Ying; Han, Junchao; Min, Hao; KRISHNA, Anurag; Chen, Yifan; Zhou, Huawei; Zhang , Xueling; Chen , Cong; Chang, Jin; Li, Can; Chen, Yifeng; Feng, Zhiqiang; Li, Zhen; Zuo, Guangzheng; Gao, Jifan; Mo, Xiaoliang; Zhang , Hong & Chu, Junhao
(2024) Homogenizing Morphology and Composition of Methylammonium-Free Wide-Bandgap Perovskite for Efficient and Stable Tandem Solar Cells. In: Advanced functional materials, 34 (37) (Art N° 2402061).

DOI: 10.1002/adfm.202402061
Handle: http://hdl.handle.net/1942/42985

Homogenizing morphology and composition of methylammonium-free wide-bandgap perovskite for efficient and stable tandem solar cells

Xinxin Lian[1], Ye Xu[2], Wei Fu[3], Rui Meng[4], Quanxing Ma[1,5], Chunyu Xu[1], Ming Luo[1], Ying Hu[1], Junchao Han[1], Hao Min[6], Anurag Krishna,[7,8,9] Yifan Chen[1], Huawei Zhou[10], Xueling Zhang[2], Cong Chen[5], Jin Chang[6], Can Li[4], Yifeng Chen[2], Zhiqiang Feng[2], Zhen Li[4], Guangzheng Zuo[3], Jifan Gao[2], Hong Zhang[1*], Xiaoliang Mo[1*], Junhao Chu[1]

[1]State Key Laboratory of Photovoltaic Science and Technology, Shanghai Frontiers Science Research Base of Intelligent Optoelectronics and Perception, Department of Materials Science, Institute of Optoelectronics, Yiwu Research Institute, Fudan University, Shanghai 200433, China.

[2]State Key Laboratory of Photovoltaic Science and Technology, Trina Solar, Changzhou 213031, China.

[3]Institute for Electric Light Sources, School of Information Science and Technology, Fudan University, Shanghai, 200433 China.

[4]State Key Laboratory of Solidification Processing, Center for Nano Energy Materials, School of Materials Science and Engineering, Northwestern Polytechnical University and Shaanxi Joint Laboratory of Graphene (NPU), Xi'an 710072, China.

[5]School of Materials Science and Engineering, State Key Laboratory of Reliability and Intelligence of Electrical Equipment, Hebei University of Technology, Tianjin 300130, China.

[6]Key Laboratory of Flexible Electronics (KLOFE), Institute of Advanced Materials (IAM) & School of Flexible Electronics (Future Technologies), Nanjing Tech University, Nanjing, China.

[7]Imec, imo-imomec, Thin Film PV Technology, Thor Park 8320, 3600 Genk, Belgium.

[8]EnergyVille, imo-imomec, Thor Park 8320, 3600 Genk, Belgium.

[9]Hasselt University, imo-imomec, Martelarenlaan 42, 3500 Hasselt, Belgium.

[10]School of Chemistry and Chemical Engineering, College of Materials Science and Engineering, Shandong Provincial Key Laboratory/Collaborative Innovation Center of Chemical Energy Storage, Liaocheng University, Liaocheng 252000, China.

*Correspondence to: hzhangioe@fudan.edu.cn (H.Z.); xlmo@fudan.edu.cn (X.L.M.)

Abstract

We present a facile and eco-friendly dimethyl sulfoxide-mediated solution aging (DMSA) treatment to control the crystallization dynamics of methylammonium (MA)-free wide-bandgap (WBG) perovskite films, enhancing film quality and morphology for high-performance tandem solar cells. Our comprehensive structural, morphological, and characterization analyses reveal that the DMSA treatment significantly enhances composition and morphology homogeneity while suppressing halide segregation. Consequently, opaque and semi-transparent MA-free WBG perovskite solar cells (PSCs) exhibit remarkable power conversion efficiencies (PCEs) of 18.28% and 17.61%, respectively. Notably, the unencapsulated DMSA-treated devices maintain 95% of the initial PCE after 900 hours of continuous operation at 55 ± 5°C. Furthermore, stacking semi-transparent DMSA-treated PSCs as top cells in a 4T tandem configuration, along with silicon heterojunction (SHJ), lead-tin (Pb-Sn) alloyed PSCs, and organic photovoltaics (OPV) as bottom cells, yields impressive PCEs of 28.09%, 26.09%, and 25.28%, respectively, for the fabricated tandem cells. This innovative approach opens new avenues for enhancing the photo-stability and photovoltaic performance of perovskite-based tandem solar cells.

Introduction

Perovskite solar cells (PSCs) are among the most promising photovoltaic technologies because of their low cost, high efficiency, and solution processability[1-3]. Significant efforts have been devoted to enhancing the power conversion efficiency (PCE) of single-junction PSCs, achieving PCE as high as 26.1%[4], closely approaching the Shockley-Queisser limit[5]. To further elevate performance, the focus has shifted on developing tandem solar cells which can effectively avoid thermalization energy losses and thus boost the theoretical PCE of PSC-based solar cells to 44.1%[6]. The integration of semi-transparent wide-bandgap (WBG) perovskite top subcells with narrow-bandgap (NBG) bottom subcells (e.g., crystalline silicon [c-Si][7], copper indium gallium selenide [CIGS][8], Sn-based PSCs[9] and organic photovoltaics [OPV][10]) is one of the most feasible strategies for fabricating tandem solar cells with both high-efficiency and industrial compatibility[11]. Currently, the iodine (I) and bromine (Br) mixed-halide strategy is the most effective approach for preparing WBG perovskite. However, the distinct ionic properties between Br and I lead to disparate crystallization behaviors in the precursor solution[12]. This often results in mixed-halide WBG perovskite films with uneven surface morphology and significant bulk composition variation, leading to non-radiative recombination, low optical transmittance below the bandgap, and stability concerns[13,14]. Consequently, there is a pressing need for innovative strategies to modulate the crystallization dynamics of WBG perovskites, aiming to achieve a homogeneous film morphology and composition.

The use of toxic solvents in preparing perovskite precursors and controlling the crystallization of wide-bandgap (WBG) perovskite films poses challenges for the green and sustainable development of PSCs[15,16]. In particular, the most commonly used *N*, *N*-dimethylformamide (DMF) solvent exerts severe adverse effects on the Disability Adjusted Life Year indicator[17] and has been restricted by the European Chemicals Agency[18]. By contrast, the versatile dimethyl sulfoxide (DMSO) poses a minimal risk to human safety and health (**Figure S1**, Supporting Information), earning the term "green solvents"[19,20]. However, the low saturation vapor pressure (0.049 kPa) of DMSO at room temperature leads to the formation of many defects and pinholes in the perovskite film under harsh crystallization kinetics[21]. Nevertheless, mixing DMSO with low-toxicity additives has emerged as an effective strategy to regulate the crystallization of WBG perovskite films for achieving high-performance, environment-friendly PSCs[22-26]. A precursor solution based on a

single green solvent is a preferable choice for sustainability[27]. Subsequently, some post-treatments, such as vacuuming[28], heat-assisted treatment[29], and gas quenching[30], have been proposed to rapidly extract residual DMSO in wet WBG perovskite intermediate films. However, these methods often fail to completely control phase separation, leading to an inhomogeneous surface morphology and composition in the resulting WBG perovskite films[31], This poses challenges for the development of highly efficient semi-transparent WBG PSCs and their tandem applications.

In this study, we employed a simple and facile approach known as DMSO-mediated solution aging (DMSA) treatment to control the crystallization process of wide-bandgap (WBG) perovskite. This treatment, utilizing a sole DMSO solvent, successfully mitigated halide segregation, resulting in a high-quality WBG perovskite film characterized by enhanced homogeneity, morphology, and transmittance. Consequently, the semi-transparent WBG PSCs treated with DMSA, featuring a bandgap of 1.77 eV, demonstrated an impressive power conversion efficiency (PCE) of 17.61%, coupled with an average transmittance of 74.22% in the near-infrared region (700-1100 nm). Furthermore, the four-terminal (4T) tandem solar cells, incorporating a silicon heterojunction (SHJ), a lead-tin (Pb-Sn) alloyed PSC, and an organic photovoltaic (OPV) bottom cell, exhibited PCEs of 28.09%, 26.09%, and 25.28%, respectively. The operational stability of the DMSA-treated PSCs witnessed a substantial improvement, attributed to the homogenization of film morphology and composition, which effectively suppressed halide segregation. This research introduces a facile and effective strategy to enhance the film quality and stability of WBG perovskites, thereby contributing to the advancement of perovskite-based tandem solar cells.

Results and discussion

Formation of morphologically homogenized WBG perovskite films with pure DMSO precursor inks

The WBG perovskite films were generally fabricated through a process involving spin coating of a mixed DMF/DMSO precursor ink followed by an antisolvent treatment (denoted as Control), as shown in **Figure 1a**. Anti-solvents, such as chlorobenzene (CB), are widely used to effectively extract DMF and/or DMSO molecules from wet perovskite intermediate films[32,33]. However, the high-volume use of toxic antisolvents is unfavorable for sustainable development. Furthermore, manipulating the crystallization of WBG perovskites using antisolvents remains a complex task due to their low formation energy for Br and high

nucleation raterate[34]. These factors contribute to the formation of mixed-halide WBG perovskite films with inhomogeneous morphologies and compositions, introducing defects and pinholes that adversely impact device efficiency and stability. Addressing these challenges, a wide processing window with a physical gas quenching method was proposed for solvent extraction during the spin-coating of WBG perovskite films, aiming to mitigate the issues associated with antisolvents[30]. Moreover, the toxicity of precursor solvents limits the industrialization of WBG perovskites and tandem solar cells. To overcome these limitations, we develop a strategy to prepare WBG perovskite films from a pure DMSO precursor ink by combining nitrogen (N_2) quenching and DMSA treatment (**Figure 1b**). For simplicity, the DMSA-treated WBG perovskite films are denoted as DMSA. The mixed DMF/DMSO precursor and the green DMSO precursor were dropped into the carrier transport layer for spin-coating, and gradient wet films were formed from center to edge under the antisolvent/mild nitrogen flow that generated the Marangoni effect[35,36]. Given that the viscosity of the DMSO solvent (2.24 mPa.s, 20 °C) was greater than that of the DMF solvent (0.92 mPa.s, 20 °C), the low surface tension of the DMSO solvent suppressed the lateral flow of the precursor. In addition, $FA_{1-x}Cs_xPbI_{1-y}Br_y$ systems ($X \geq 30\%$ and $Y \geq 30\%$) with film thicknesses greater than 300 nm are subjected to severe compressive strain during immediate annealing, as reported in literature[37], leading to the formation of inhomogeneous wrinkles on the film surface. This result is consistent with the characterization of the control films and pure DMSO perovskite films with different concentrations on bare glass by optical microscopy and step profiler in **Figure S2 and S3** (Supporting Information). Meanwhile, the high viscosity DMSO reflux was also relatively sluggish[21], indicating that if not enough time was available to repair the inhomogeneous films under the surface tension gradient, resulting in the unsatisfactory efficiency of the WBG-PSCs (**Figure S4**, Supporting Information). Although volatilization has been referred to as a wet-film destabilizing mechanism, the destabilization can be reversed by properly controlling the intensity of Marangoni reflux[36]. The *in-situ* absorption shows that the DMSA-treated perovskite films had relatively modest absorption during the 60-second aging process, indicating that this approach was effective in slowing down the crystal growth and forming a homogeneous film (**Figure S5(a) and (b)**, Supporting Information). Additionally, the films in the thermodynamically and kinetically destabilized state are unstable[38], resulting in a quenching effect when the control wet-film was immediately placed on the hot bench (**Figure S5(c)**,

Supporting Information). In contrast, the stability of the *in-situ* PL annealing spectra of the DMSA-treated films is relatively favorable as shown in **Figure S5(d)** (Supporting Information), thus indicating superior thermal stability of the DMSA-treated films. A schematic of the in-situ setup as illustrated in **Figure S6** (Supporting Information). As depicted in **Figure 1c,** the control and the DMSA-treated perovskite films were observed by optical microscopy, and it was found that the surface of the DMSA-treated films was relatively smooth and without obvious wrinkles. For WBG perovskite solar cells, the inhomogeneous wrinkles on the film surface can lead to severe nonradiative recombination and promote phase separation[12], which is detrimental to the development of tandem solar cells. Consequently, DMSA-treated perovskite films under Marangoni reflux offer a promising solution, yielding assembled perovskite films with a homogeneous morphology and providing a novel approach for the preparation of high-quality WBG perovskite films.

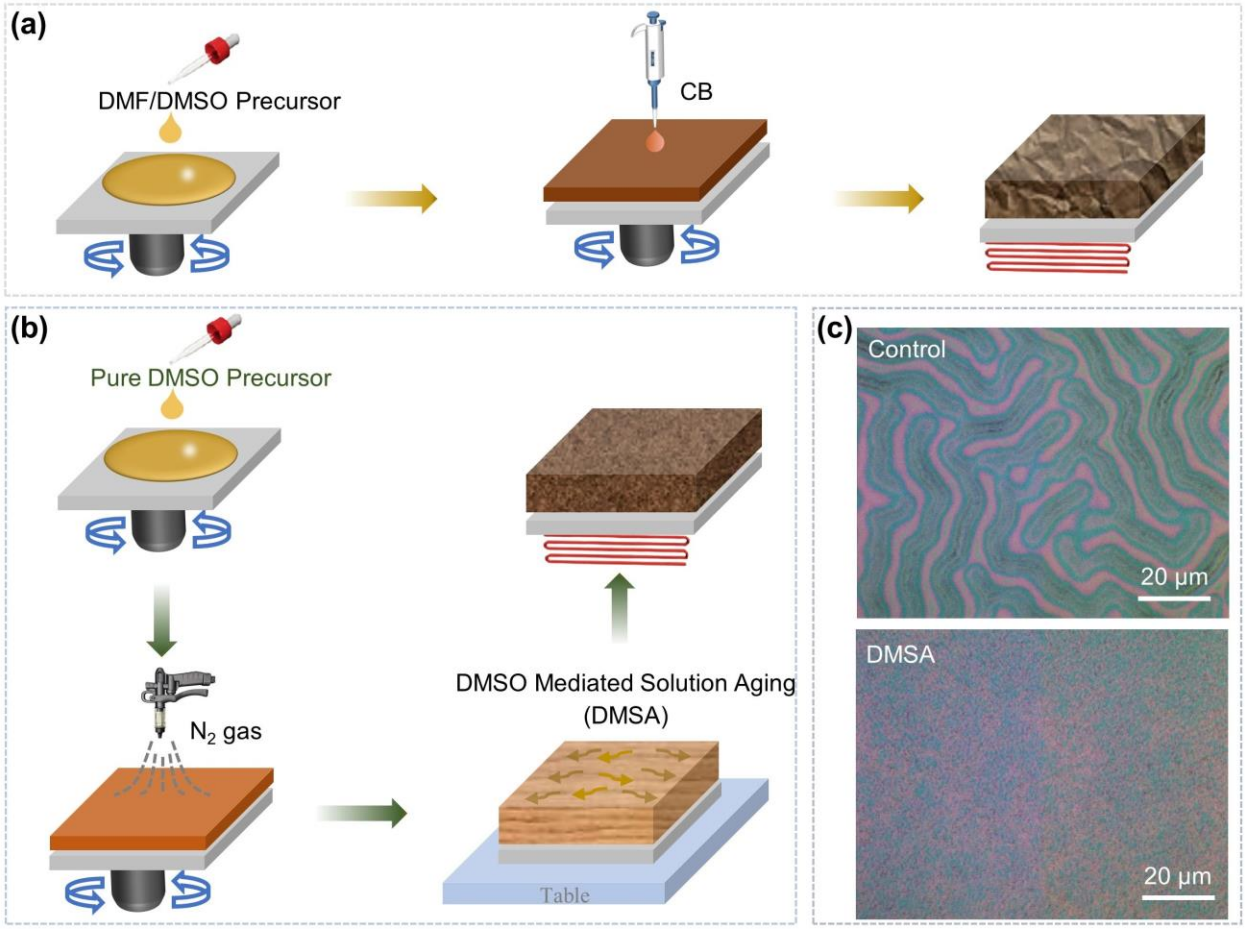

Figure 1. Schematic diagram of the fabrication process of perovskite films. a) The conventional one-step deposition of WBG perovskite films from mixed DMF/DMSO precursor ink along with antisolvent quenching.

b) The preparation of WBG perovskite films from pure DMSO precursor ink using nitrogen (N_2) quenching and DMSO-mediated solution aging (DMSA) treatment. c) Top-view optical microscopic images of the control and DMSA-treated WBG perovskite films.

Morphology and optical properties of WBG perovskite films

The homogeneous surface morphology and high transparency of WBG perovskite films are decisive factors for achieving efficient semi-transparent top cells and tandem cells. The surface morphologies of the control perovskite films were investigated by scanning electron microscopy (SEM) as shown in **Figure 2a**. Numerous wrinkles appeared on the surface of the control samples, and unevenness was clearly observed in the cross-sectional (**Figure S7**, Supporting Information). The SEM localized magnified of the control perovskite films showed that the grain size has a significant discrepancy at the peaks and valleys of the wrinkles (**Figure S8(a)**, Supporting Information). In contrast, the grain size of the DMSA film appeared to be relatively homogeneous at the peaks and valleys of the wrinkles and no obvious defects were seen in the valley (**Figure S8(b)**, Supporting Information). The wrinkles of the WBG perovskite films were mainly caused by the size mismatch between I (2.20 Å) and Br (1.96 Å) in the mixed-halogen perovskites that led to internal compressive stress relaxation during pre-crystallization and annealing[39,40]. The root-mean-square (RMS) roughness of the control perovskite films was calculated to be 77.3 nm (**Figure 2b**), and the average altitude gap between the peak and valley of the wrinkles in control perovskite films was about 280 nm (**Figure 2c**). Many defects were trapped in the wrinkle valleys, which was detrimental to crystal growth and shortened the carrier diffusion length[31]. The DMSA-treated WBG perovskite film was smoother and more homogeneous than the control perovskite film (**Figure 2d**), and the crystallinity of the films was improved under the modulation of Maragoni as indicated by XRD analysis (**Figure S9**, Supporting Information). The RMS roughness of the DMSA-treated perovskite film was reduced to 10.5 nm, as indicated in **Figure 2e**, and the height distribution was almost within 30 nm, which is significantly lower than the control sample (**Figure 2f**). Tensile and compressive strains have a crucial influence on the morphology of perovskite films[41]. The strains of the control and DMSA-treated perovskite films were investigated by employing depth-resolved grazing incident X-ray diffraction (GIXRD) technique with 2θ-$\sin^2\psi$ method[42]. The scattering peaks of the control film gradually shifted to left by varying Ψ from 0° to 35°, indicating the

increasing of crystal plane distance and bearing tension stress of the control film as shown in **Figure S10(a)** (Supporting Information). However, the scattering peaks of the DMSA-treated perovskite films exhibited little shift during varying Ψ from 0° to 35° as shown in **Figure S10(b)** (Supporting Information), which indicated that the residual stress in the perovskite films were diminished with less strain gradient and the closer lattice distance, leading to an almost homogeneous surface morphology of the films. The perovskite film stress was calculated by fitting the 2θ as a function of $\sin^2\psi$, of which the slope of the fitting line represents the residual strain as shown in **Figure S10(c)** (Supporting Information). The higher residual stress on the film surface implies more severe lattice distortion, causing more defects at the interfaces and more roughness on the film surface[43]. For WBG PSCs, the surface roughness of the film can lead to severe nonradiative recombination, which is detrimental to the efficiency and stability[12]. Notably, the microscopically wrinkled films showed a matte appearance on the macroscopic scale, whereas the microscopically smooth films were polished and transparent on the macroscopic scale, as shown in **Figure 2g**. The average transmittance of the DMSA-treated semi-transparent WBG perovskite film was 83.94% in the near-infrared region (700-1100nm) as shown in **Figure 2h**, which is more conducive to the harvesting of sunlight by the bottom cell of tandem solar cells.

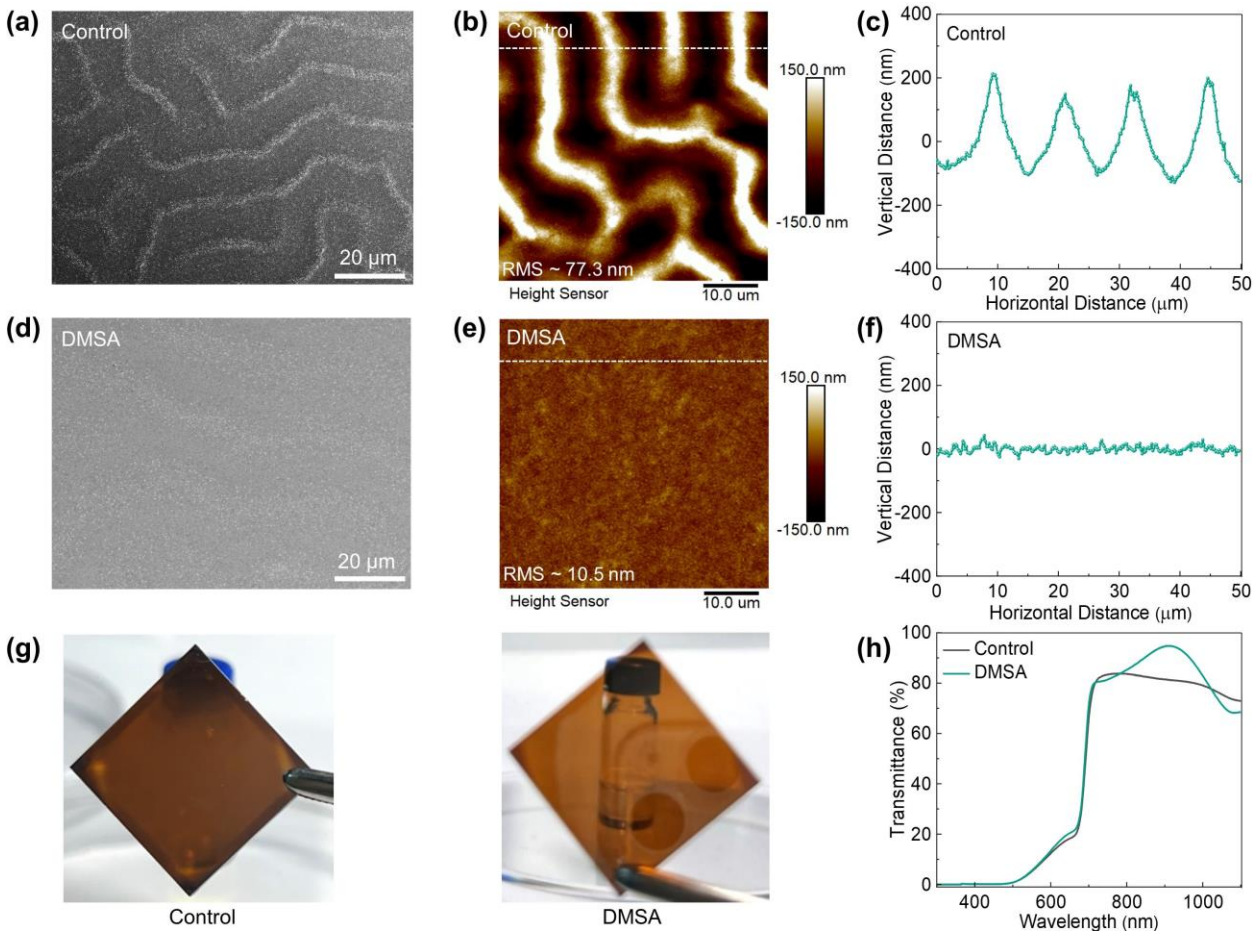

Figure 2. Surface morphology and transparency of WBG perovskite films. a) SEM images and b) AFM images of control WBG perovskite films. c) Corresponding surface altitude deviation in Figure 2b. d) SEM images and e) AFM images of DMSA-treated perovskite films. f) Corresponding surface altitude deviation in Figure 2e. g) Photograph images and h) UV-vis transmittance spectra of control and DMSA-treated perovskite films.

Effect of morphology and composition on photo-stability and carrier transport

WBG perovskite films are usually based on a mixture of I-Br halides[40]. In principle, the radius of the Br- is smaller than I- and the addition of abundant Br- makes the perovskite films increasingly stable because of the Pb–Br bond is stronger than the Pb–I bond[30]. However, Br content greater than 20% is highly susceptible to inducing severe phase separation under thermodynamic and kinetic destabilized states[44], which is a major constraint in limiting the performance enhancement of WBG PSCs[45]. The *in-situ* photoluminescence (PL) and absorption spectra of the WBG perovskite films were measured during the spin-coating process, indicating that the green DMSO precursor ink exhibited a faster nucleation and slower crystallization, and the significant delay in crystallization resulted in reorganization of the morphology and enhanced crystallization (**Figure S11**, Supporting Information). Steady-state PL microscopy was performed randomly

over a micro-size region of 50 μm × 50 μm in the control and DMSA-treated WBG perovskite films, as shown in **Figure 3**. The pronounced discrepancy in the PL intensity of the peaks and valleys of the wrinkles was observed owing to the control films showed inhomogeneous morphology and multiple wrinkles. The PL single-point spectra in **Figure 3c** of the control film correspond to the positions of the random markers of different PL intensities in **Figure 3a** (C_1 denotes the red region, C_2 denotes the yellow region, C_3 denotes the green region and C_4 denotes the blue region). Gaussian fitting was employed to obtain accurate PL peak positions as shown in **Figure S12** (Supporting Information). The PL intensity was the strongest in the C_1 red region of the wrinkle peak at 705.25 nm, followed by the C_2 yellow region with the PL peak at 700.63 nm. The PL peak of the C_3 green region at the edge of the yellow region was at 696.14 nm, and the PL peak of the C_4 blue region at the valley of the wrinkles was at 691.39 nm. The PL peaks gradually decreased from the peak to valley of the wrinkles with a blue shift, indicating the phase separation of the control perovskite film. In contrast, the PL mapping of the DMSA-treated perovskite films are homogeneous (**Figure 3b**), with fewer defects and compositional segregation. The improvement of the film quality could effectively suppress nonradiative recombination[12]. The PL spectra of the DMSA-treated perovskite film were obtained by randomly selecting PL points at D_1, D_2, D_3 and D_4, as shown in **Figure 3d**. The spectra confirmed that the PL peaks were stably located around 700 nm (**Figure S13**, Supporting Information), and the peak intensities were homogeneous in the DMSA-treated perovskite film. The inhomogeneity of the PL spectra of the control perovskite films was aggravated after 24 h of photoaging (**Figure S14**, Supporting Information), and the PL intensity of the control film decreased dramatically and intermediate phase peaks were generated. According to previous reports[46-48], charge accumulation caused by insufficient carrier extraction is the main reason for the energy loss in WBG PSCs. Given the transfer of electrons/holes generated at the interface towards adjacent transport layers, the time-resolved photoluminescence (TRPL) measurement was employed to investigate the carrier transport. As shown in **Figure S15** (Supporting Information), the DMSA-treated perovskite film exhibited a faster PL decay than that of control perovskite films when the hole and electron quenchers were used. According to the carrier transport principle[46,49], DMSA-treated perovskite films with a homogeneous surface morphology usually facilitated device performance because of the highly ordered lattice that reduced disordered electronic states and accelerated

charge transport (**Figure 3f**). Conversely, the inhomogeneous morphology and composition of the control films lead to a significant charge accumulation in the high-trapping-density regions[12], further accelerating halide segregation in WBG perovskite films and limiting their device performance (**Figure 3e**). Additionally, the TRPL spectra of perovskite films on glass were also examined to assess the charge carrier lifetimes. The DMSA-treated perovskite film yields a longer average carrier lifetime (τ_a) of 348 ns with respect to that of the control film (τ_a= 183 ns) (**Figure S16**, Supporting Information), which indicated the improved WBG film quality with lower defect density. Therefore, homogenizing the morphology and composition of mixed-halide WBG perovskite films through the DMSA treatment is favorable for enhancing device stability and tandem cell development.

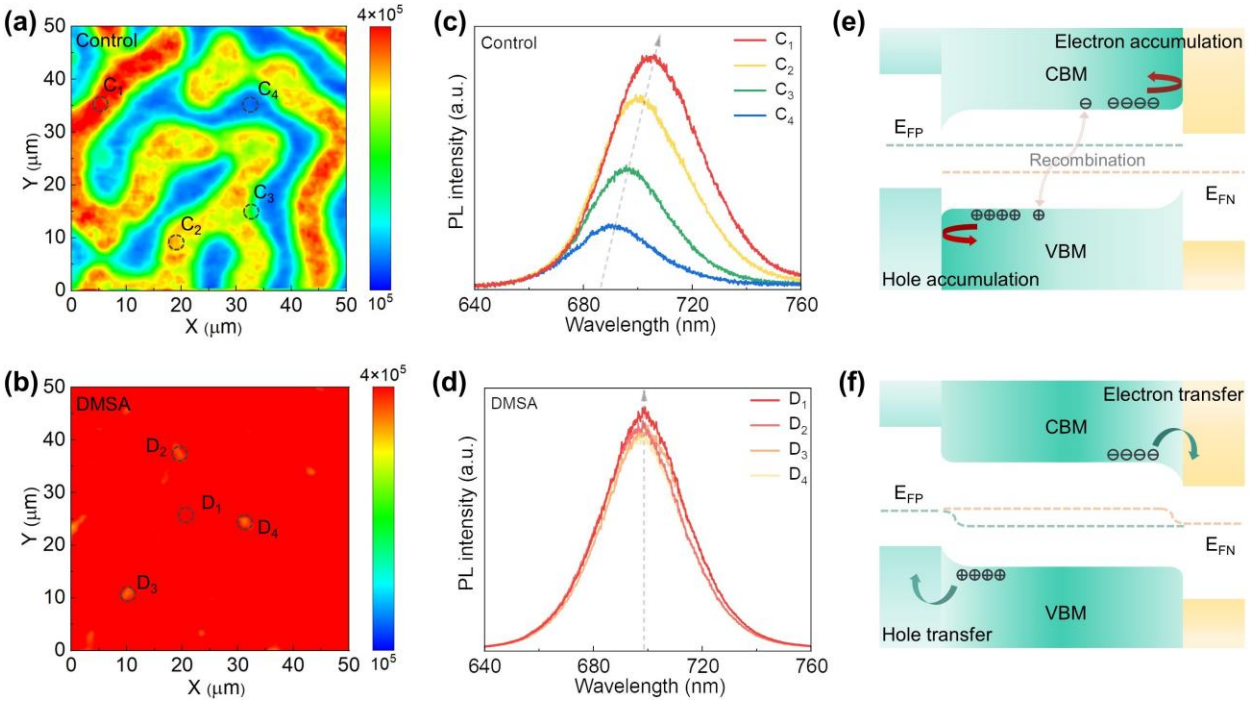

Figure 3 Homogeneity and photo-stability of WBG perovskite films. PL mapping of the a) control and b) DMSA-treated WBG perovskite films. c) The PL single-point spectra of the control film correspond to the marked positions ($C_1 \sim C_4$) in Figure 3a. d) The PL single-point spectra of the DMSA-treated film correspond to the marked positions ($D_1 \sim D_4$) in Figure 3b. Schematic illustrations of band alignments in e) control and f) DMSA-treated PSCs under illumination. CBM conduction band minimum, VBM valence band maximum, E_{FN} electron quasi-fermi level, E_{FP} hole quasi-fermi level.

Photovoltaic performance and operational stability of WBG PSCs.

Homogenized and wrinkle-free morphology of the DMSA-treated WBG PSCs with the p-i-n inverted planar structure of ITO/NiO_x/SAM/perovskite/PCBM/AZO/ALD-SnO_2/Ag as shown in **Figure 4a**. The SAM layer

consisted of mixed 2PACz and MeO-2PACz, where 2PACz is [2-(9*H*-carbazol-9-yl)ethyl]phosphonic acid and MeO-2PACz is [2-(3,6-dimethoxy-9*H*-carbazol-9-yl)ethyl]phosphonic acid. The inverted planar WBG PSCs displayed negligible hysteresis, as indicated in **Figure 4b**. The superior WBG PSCs subjected to DMSA treatment displayed a champion PCE of 18.28% under reverse scan, with V_{oc} of 1.24 V, J_{sc} of 17.90 mA cm^{-2}, and FF of 82.07%, which are among the highest values reported for WBG PSCs with green solvents and Eco-friendly fabrication processes (**Table S1**, Supporting Information). The DMSA-treated PSCs showed a stabilized PCE of 18.03% measured over 300 s (**Figure 4c**), which was consistent with the average PCE of the 22 devices (**Figure S17**, Supporting Information). The external quantum efficiency (EQE) spectra of the PSCs were shown in **Figure 4d**, which indicated that the control and DMSA-treated PSCs had high quantum yields in the range of 300-700 nm (**Figure 4e**). This increment corresponded to a significantly remarkable increase in the integrated J_{sc} from 16.94 mA cm^{-2} to 17.61 mA cm^{-2} after DMSA treatment. The bandgaps of both control and DMSA-treated perovskite films were 1.77 eV by determining from the derivative of the EQE spectra, which is consistent with the results obtained from the UV-visible absorption spectra and the Tauc plots (**Figure S18**, Supporting Information). Large-area devices (aperture area of 1.21 cm^2 and mask of 1.0 cm^2) were also fabricated to assess the effects of the homogeneity in morphology and composition on industrialized production (**Figure 4f**). The PCE of the large-area DMSA-treated PSCs was 17.20% (V_{oc} = 1.22 V, J_{sc} = 17.66 mA cm^{-2}, and FF = 80.15%) under reverse scan and superior to the PCE of the control device (PCE = 14.39%, V_{oc} = 1.20 V, J_{sc} = 15.02 mA cm^{-2}, and FF = 79.76%), and the statistical data of the photovoltaic parameters based on 26 individual perovskite cells are shown in **Figure S19** (Supporting Information). These findings underscore the contribution of homogeneous morphology and composition to the scalability of large-area PSCs and tandem solar cells. Next, the long-term stability of the devices was evaluated. As shown in **Figure 4g**, the unencapsulated DMSA-treated devices maintained 95% of initial PCE after 900 hours continuous operation under a white LED lamp in the wavelengths range of 385 nm ~ 800 nm (**Figure S20**, Supporting Information) and at 55 ± 5°C, while the control devcies decreased by 30%. Meanwhile, thermal stability was further investigated by aging the devices at 85°C (**Figure S21**, Supporting Information). After 34 days of thermal aging, the performance of the DMSA PSCs decreased by 10%, and that of the control samples was reduced by 40%. The enhanced

operational stability and thermal stability were attributed to the homogeneous morphology and composition of the perovskite film and the low concentration of defects in the perovskite absorption layer.

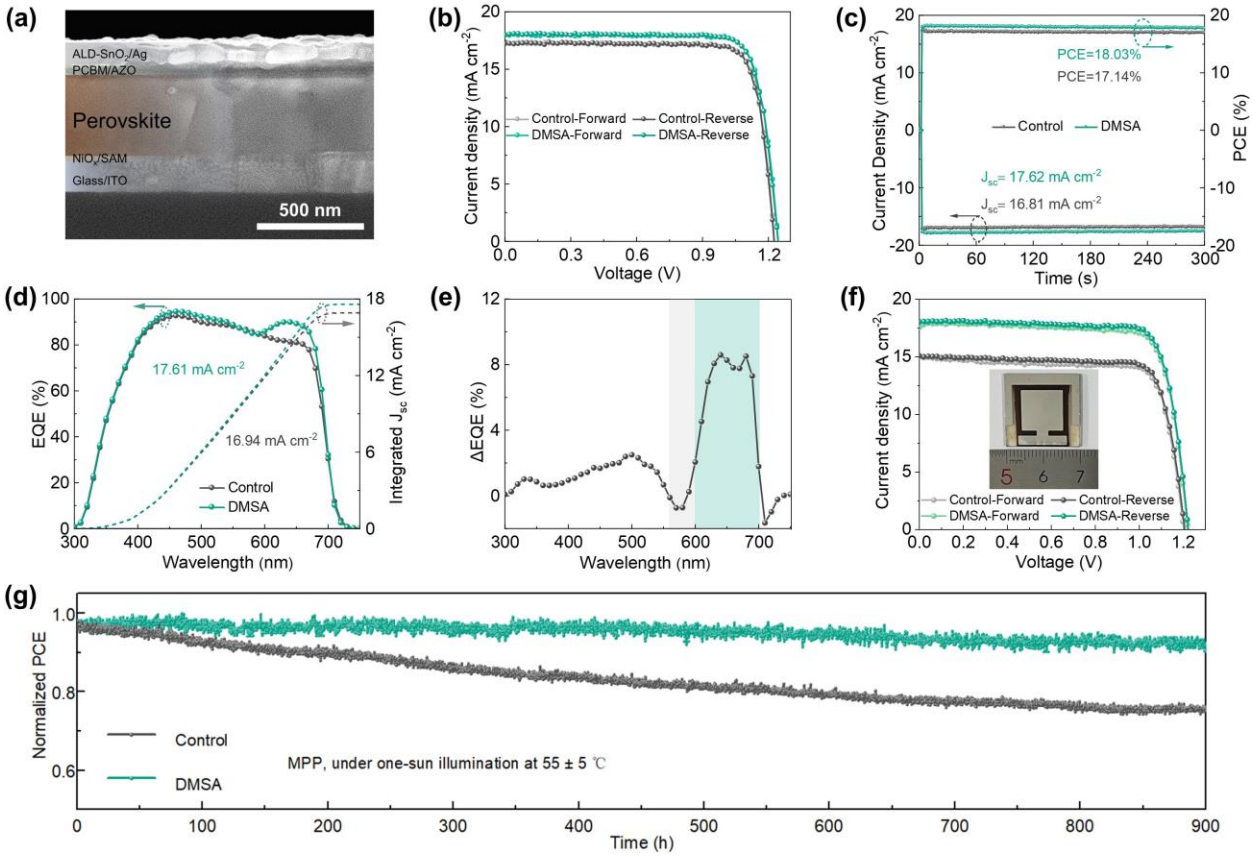

Figure 4 Photovoltaic performance and stability of opaque PSCs. a) Cross-sectional SEM image of a DMSA-treated PSC. b) *J-V* curves of control and DMSA-treated PSCs. c) Steady-state J_{sc} and PCE of control and DMSA-treated PSCs. d) EQE spectra and integrated J_{sc} of control and DMSA-treated PSCs. e) Difference of EQE spectra of control and DMSA-treated PSCs. f) *J-V* curves of large-area control and DMSA-treated PSCs with an area of 1 cm^2. The inset shows the photograph image of the large-area device. g) Normalized PCE of the unencapsulated control and DMSA-treated devices measured at maximum power point under continuous one-sun illumination at 55 ± 5°C in N_2 atmosphere.

Semi-transparent PSCs and tandem applications

The top opaque Ag electrodes were substituted for transparent electrodes, which was necessary for the tandem cell to utilize the photon harvesting sufficiently and efficiently. Indium zinc oxide (IZO) electrodes were obtained by magnetron sputtering, which can ensure conductivity and transmittance to reduce parasitic losses. The device configuration of the semi-transparent device was shown in **Figure 5a**. The average transmittance of the semi-transparent DMSA-treated WBG PSCs was 74.22% in the near-infrared region (700-1100 nm) as indicated in **Figure 5b**. The PCE of the semi-transparent DMSA-treated PSCs was 17.61%

(V_{oc} = 1.27 V, J_{sc} = 17.13 mA cm^{-2}, and FF = 81.01%) under reverse scan in **Figure 5c** and the statistical data as shown in **Figure S22** (Supporting Information). The PCE of the semi-transparent DMSA-treated PSCs was superior to that of the control devices (PCE = 16.05%, V_{oc} = 1.24 V, J_{sc} = 16.75 mA cm^{-2} and FF = 77.27%). Designing effective bottom cell structures is crucial to realize efficient tandem solar cells with absorption edges beyond the perovskite. Afterward, 1.77 eV semi-transparent DMSA-treated PSCs were stacked with a 1.1 eV SHJ bottom cell, and the current output was maximized by increasing the antireflective film to reduce the light loss. As a result, a high J_{sc} was obtained for the SHJ devices under high-transmittance DMSA-treated devices, as shown in **Figure 5d**. The efficiency of the 4T SHJ-PSC tandem device exceeded 28%. The EQE spectra revealed that the integrated J_{sc} of the DMSA-treated PSCs and filtered SHJ devices were 16.91 mA cm^{-2} and 18.64 mA cm^{-2}, respectively, which are consistent with the J_{sc} values in the *J-V* curves in **Figure 5e**. Meanwhile, an analogous 4T structural design strategy was applied to the NBG Sn-Pb PSCs and OPV bottom cells. The 1.24 eV Sn-Pb PSC with exceptional performance mechanically stacked with a 1.77 eV PSC to fabricate PSC-PSC 4T tandem cell, which showed an outstanding PCE of 26.09% (**Figure 5f**). The EQE spectra of the filtered Sn-Pb PSC by the DMSA-treated PSC device were shown in **Figure 5g**. The integrated J_{sc} was 12.51 mA cm^{-2}, which is slightly lower than the J_{sc} in the *J-V* curve because of the mismatch of the bandgap. The OPV-PSC 4T tandem system adopted full-solution processing technology, which effectively avoided the damage of the upper layer solution to the bottom layer film and improved the photon harvesting capacity with 25.28% efficiency (**Figure 5h**) and the EQE spectra of the filtered OPV by the DMSA-treated PSC device were shown in **Figure 5i**. In short, the DMSA treatment play a crucial role in achieving high-performance perovskite-based tandem solar cells. The detailed photovoltaic parameters were summarized in **Table 1** and **Table S2** (Supporting Information).

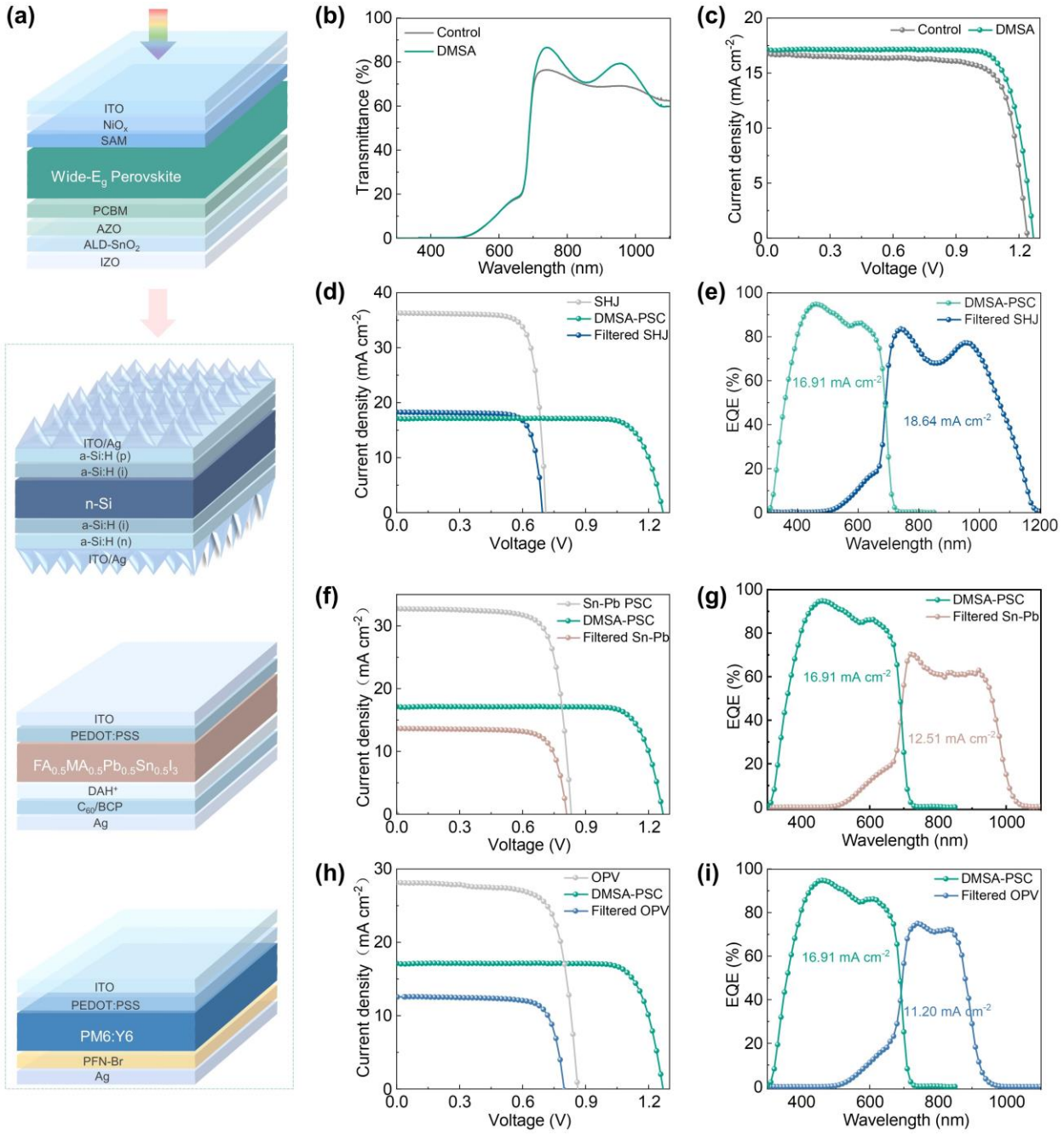

Figure 5 Photovoltaic performance of semi-transparent PSCs and tandem solar cells. a) Schematic device configuration of 4T perovskite-based tandem solar cells. b) UV-vis transmittance spectra and c) *J-V* curves of semi-transparent control and DMSA-treated PSCs. *J-V* characteristics and EQE spectra of semi-transparent DMSA-treated PSC top cell and filtered silicon heterojunction (SHJ) bottom cell (d, e), filtered NBG Sn-Pb perovskite bottom cell (f, g), and filtered OPV bottom cell (h, i) as well as their 4T tandem cells.

Table 1. Photovoltaic parameters of semi-transparent DMSA-treated PSCs and tandem solar cells.

Cells	V_{oc} (V)	J_{sc} (mA cm^{-2})	FF (%)	PCE (%)
Semi-transparent PSCs	1.27	17.13	81.01	17.61
Filtered SHJ	0.69	18.98	79.32	10.48
PSC-SHJ 4T				28.09
Filtered NBG PSCs	0.81	13.65	75.56	8.48
PSC-PSC 4T				26.09
Filtered OPV	0.80	12.39	77.39	7.67
PSC-OPV 4T				25.28

Conclusion

In summary, we present an environmentally friendly DMSA strategy designed to control the crystallization process of WBG perovskite films, resulting in films characterized by homogeneous morphology and composition distribution. This approach enhanced the photo-stability and transparency. The WBG perovskite solar cells (PSCs), with a bandgap of 1.77 eV, demonstrate remarkable power conversion efficiencies (PCEs) of 18.28% and 17.61% for opaque and semi-transparent configurations, respectively. These semi-transparent cells maintain an impressive average transmittance of 74.22% in the near-infrared region. The unencapsulated DMSA-treated devices maintained 95% of initial PCE after 900 hours continuous operation at 55 ± 5°C. Moreover, stacking semi-transparent DMSA-treated PSCs as the top cells in a 4T tandem configuration, alongside silicon heterojunction (SHJ), lead-tin (Pb-Sn) alloyed PSCs, and organic photovoltaics (OPV) as bottom cells, results in remarkable PCEs of 28.09%, 26.09%, and 25.28%, respectively, for the fabricated tandem cells. This research introduces a straightforward yet highly effective strategy to elevate the quality and stability of WBG perovskite films, paving the way for sustainable production and future advancements in perovskite-based tandem solar cells.

Methods

Materials. Commercial ITO substrates (15 Ω sq^{-1}) with 20 mm × 20 mm dimension were purchased from Advanced Election Technology Co., Ltd. NiO_x nanoparticles (NPs) were synthesized according to previous work[50]. Dimethylammonium iodide (DMAI), cesium iodide (CsI) and formamidinium iodide (FAI) were purchased from Greatcell Solar. Self-assembled monolayer (SAM) of 2PACZ and MeO-2PACZ and bathocuproine (BCP) were purchased from Xi'an Polymer Light Technology. Lead iodide (PbI_2), lead bromide ($PbBr_2$) and lead chloride ($PbCl_2$) were purchased from Advanced Election Technology Co., Ltd. [6,6]-phenyl-C61-butyric acid methyl ester (PCBM) were purchased from Nano-C. Aluminum doped zinc oxide (AZO) nanoparticle inks and all solvents were anhydrous solvents from Sigma-Aldrich. Precursors of tetrakis (dimethylamino) tin (IV) (99.9999%, Nanjing Ai Mou Yuan Scientific Equipment). IZO sputtering target was purchased from Zhongsheng Heng'an.

Hole-transport layer (HTL) fabrication. The pre-patterned ITO substrates were cleaned and treated with UV-ozone for 15 min. The 20 mg ml^{-1} NiO_x NP aqueous ink onto ITO substrates at 4000 r.p.m. for 30 s and annealed at 100°C for 10 min under ambient conditions. Then, the obtained NiO_x films were immediately transferred into a nitrogen-filled glovebox. A self-assembled monolayer of mixed-solution 2PACz and MeO-2PACz (1 mM in ethanol, volume ratio 3:1) at 4000 r.p.m. for 30 s, followed by 10 min of annealing at 100 ℃.

Perovskite absorber layer fabrication. The perovskite absorber layers were deposited in the N_2-filled glove box with controlled H_2O and O_2 levels below 0.1 ppm, and the temperature was monitored to be 21~23°C. The control precursors for 1 M $Cs_{0.3}FA_{0.6}DMA_{0.1}Pb(I_{0.7}Br_{0.3})_3$ perovskites were prepared by dissolving the PbI_2, $PbBr_2$, $PbCl_2$, CsI, FAI, and DMAI in DMF/DMSO solvents (4/1 in volume), and the DMSA precursors for 1.4 M $Cs_{0.3}FA_{0.6}DMA_{0.1}Pb(I_{0.7}Br_{0.3})_3$ perovskites powder dissolved in DMSO solvents. 50 μL of perovskite precursor was dropped onto the HTL substrate. The substrate was spun at 2000 r.p.m. for 15 s with an acceleration of 1000 r.p.m. s^{-1} at first, and then at 4000 r.p.m. for the 45 s with an acceleration of 2000 r.p.m. s^{-1}. For control device, during the second spin-coating step, 150 μl CB was dropped onto the perovskite film at 25 s before the end of the process. The control perovskite wet-films were immediately annealed at 100°C for 30 min. For DMSA device, the nitrogen gun was vertically positioned 5 cm above the top of the substrates and the gas flow started after 30 s of the spin and duration of 20 s when the gas flow pressure was 30 psi. Subsequently, the DMSA wet-films were aged at room temperature for 1 min and then annealed at 100°C for 30 min.

Electron-transport layer (ETL) fabrication. The 23 mg ml^{-1} of $PC_{61}BM$ solution in CB was spin-coated at 2,500 r.p.m. for 40 s and then annealed at 70°C for 10 min. AZO solution (2.5 wt% AZO nanoparticle solution: IPA=3:20 by volume) was spin-coated at 2000 r.p.m. for 30 s. Thereafter, 160 cycles of SnO_x were deposited on top of the AZO film at 100°C in an ALD reactor (MNT-S100-L4S1, Jiangsu MNT Micro and Nanotech Co., LTD.). Each ALD cycle consists of a H_2O vapor dose of 0.02 s, followed by a purge of 25 s, then a TDMA dose of 0.2 s, followed by a purge of 20 s.

Back electrode fabrication. For opaque devices, the 100 nm Ag electrode with an active area of 0.1017 cm^2 was deposited by thermal evaporation. For semi-transparent devices, 100 nm IZO electrode was sputtered in TRP450 system with a processing pressure of 0.5 Pa, sputtering power was100 W and the gas flow was 30 sccm of argon gas and Ag grids were prepared around the IZO film.

Fabrication of the silicon bottom cell. SHJ bottom cells were fabricated on wafers (n-doped, resistivity 1~5 Ω cm^{-1}). The texturing process was done in an alkaline solution to get randomly distributed pyramids.

Subsequently, the wafers were cleaned in RCA1 and RCA2 solution. Prior to the PECVD depositions, the wafers were dipped in 5% hydrofluoric acid solution to remove the native oxide layer. Then, the wafers were passivated on both sides with an intrinsic layer of amorphous silicon (i) followed by the doped silicon amorphous layers, n on the front and p on the back. The i, p, and n layers were deposited in a PECVD cluster with a thickness of 8, 7, 15 nm respectively. The back contact of the SHJ was realized by sputtering sequentially ITO and Ag (150 and 250 nm, respectively). After the In_2O_3:H top contact deposition, metal fingers are screen printed using a commercial Ag paste and immediately annealed at 200°C for 15 min in ambient air.

Fabrication of the NBG PSC bottom cell. Diluted PEDOT:PSS (PEDOT:PSS:IPA=1:1, v/v) was spin-coated on the ITO substrate at 4000 r.p.m. for 30 s, followed by annealing at 150°C for 10 min. The perovskite precursor solution was spin-coated onto the PEDOT:PSS with 1000 r.p.m. for 10 s and 4000 r.p.m. for 40 s. 200 μL EA was dropped onto the substrates during the second step. The prepared perovskite films were first annealed at 60°C for 2 min, and then 100°C for 10 min. For the DAH^+ post-treatment devices, DAH^+ solution was spin-coated onto the perovskite film at 4000 r.p.m. for 30 s, followed by annealing at 75°C for 10 min. The perovskite films were then transferred into a vacuum chamber for thermal evaporation. C_{60} (40 nm), BCP (7 nm) and Ag (100 nm) were sequentially deposited on the perovskite films.

Fabrication of the OPV bottom cell. The PEDOT:PSS solution was spin-coated on the top of ITO with 2000 r.p.m. for 40 s, followed by annealing at 150°C for 15 min in air. The active layer of PM6:Y6 (w/w=1/1.2, in chloroform) was spin-coated with 3500 r.p.m. for 40 s and annealing at 100°C for 5 min. The PFN-Br (0.5 mg/mL, in methanol) layer was spin-coated on the top of active layer with 2000 r.p.m. for 40 s. The Ag contact (100 nm) was deposited through a shadow mask under a pressure of 5×10^{-4} Pa.

Characterizations. The surface morphology of the perovskite films was measured using field emission scanning electron microscope at 10 kV (FESEM, JSM-7800F) and optical microscope (Olympus BX53M). The surface roughness of the thin film was examined by Atomic Force Microscopy (AFM, Bruker) in tapping mode and the cantilevers (T: 650 nm, L:115 μm, W: 25μm, f: 70 kHz, k: 0.4 N/m). The absorption and transmittance spectra of perovskite films were measured by a *UV-vis* spectrophotometer (Varian Carry 500 spectrometer, USA). The thicknesses of the perovskite films were determined with a JS10A step profiler. The XRD data were obtained by using a Bruker D8 Advance diffractometer. The PL mapping of the perovskite films was measured using Wayne[3]labs Instruments & Solutions MAPS-Raman & FLIM at CNI Laser MSL-U-532-100 mW (HORIBA). The *in-situ* absorption spectra were measured using an ISAS-HI001 system (Nanjing Ouyi Optoelectronics Technology). A Hamamatsu EQ-99-FC:DF001 laser-driven broadband light source was used as the white-light source. The *in-situ* PL spectra were measured using an ISPL-HI001 system with a 445 nm laser (Nanjing Ouyi Optoelectronics Technology). The time resolved PL (TRPL) spectra were acquired at 10 MHZ using OYSL Photonics SC-PRO with 1 uw power on the sample at the laser wavelength of 532 nm. The current density-voltage (J-V) characteristics of the devices were measured in the N_2-filled glove box with controlled H_2O and O_2 levels below 0.1 ppm. The light intensity was adjusted to AM 1.5 G one sun (100 mW cm^{-2}) with an NIM calibrated standard silicon solar cell. A Keithley 2450 is used for the current-voltage scan by applying an external voltage bias and measuring the response current with a scan rate of 20 mV/s in the range of -0.1~1.4 V or 1.4~-0.1 V. The device area was 0.1017 cm^2 (R=0.18 cm). The cells were masked with a black metal mask with an area of 0.0804 cm^2 (R=0.16 cm). External quantum efficiency (EQE) spectra were recorded with a commercial apparatus (Arkeo-Ariadne, Cicci Research s.r.l.) based on a 300 W Xenon lamp. The operational stability of the

devices was measured under a white light-emitting diode lamp in the wavelengths range of 385 nm ~ 800 nm. The light intensity is around 100 mW cm^{-2}, and the actual current is adjusted according to in-time calibration results from the silicon solar cell.

Acknowledgments

This work was supported by Shanghai Pujiang Program (22PJ1401200) and the National Natural Science Foundation of China (No. 52302229).

Author contributions

H.Z., X.L.M., and J.H.C. supervised the project. H.Z. and X. L. convinced the idea. X. L. fabricated the WBG PSCs and conducted most of the characterizations. Y.X., X.L.Z., Y.F.C., Z.Q.F., and J.F.G. were responsible for the fabrication of SHJ and characterization of PSC-SHJ tandem cells. W.F. and G.Z.Z. were responsible for the fabrication of OPV and characterization of PSC-OPV tandem cells. R.M., C.L. and Z.L. were responsible for the fabrication of Sn-Pb NBG PSCs and characterization of PSC-PSC tandem cells. Q.X.M., M.L., Y.F.C., Y. H., J.C.H. were participated in the optimization of WBG PSCs. H.M. and J.C. were responsible for the in-situ PL/UV-vis characterizations of WBG perovskite film formation. H.W.Z. conducted the SEM characterization of WBG perovskite films. C.Y.X., A.K., and C.C. were involved in the results discussion. L.X. wrote the first draft, H.Z. and A.K. revised the manuscript. All authors contributed to the proofs of the manuscript.

Conflict of Interest

The authors declare no conflict of interest.

Data Availability Statement

The data that support the findings of this study are available from the corresponding author upon reasonable request.

References

1 Park, S. M. *et al.* Low-loss contacts on textured substrates for inverted perovskite solar cells. *Nature* **624**, 289-294, (2023).

2 Cheng, J. *et al.* Wide-Band-Gap (2.0 eV) Perovskite Solar Cells with a V_{OC} of 1.325 V Fabricated by a Green-Solvent Strategy. *ACS Applied Materials & Interfaces* **15**, 23077-23084, (2023).

3 Caprioglio, P. *et al.* Open-circuit and short-circuit loss management in wide-gap perovskite p-i-n solar cells. *Nature Communications* **14**, 932, (2023).

4 Liang, Z. *et al.* Homogenizing out-of-plane cation composition in perovskite solar cells. *Nature* **624**, 557-563, (2023).

5 Wang, Z., Song, Z., Yan, Y., Liu, S. & Yang, D. Perovskite-a Perfect Top Cell for Tandem Devices to Break the S-Q Limit. *Advanced Science* **6**, 1801704, (2019).

6 Wang, J., Liu, H., Zhao, Y. & Zhang, X. Perovskite-based tandem solar cells gallop ahead. *Joule* **6**, 509-511, (2022).

7 Wang, X. *et al.* Long-chain anionic surfactants enabling stable perovskite/silicon tandems with greatly suppressed stress corrosion. *Nat Commun* **14**, 2166, (2023).

8 Jošt, M. *et al.* Perovskite/CIGS Tandem Solar Cells: From Certified 24.2% toward 30% and Beyond. *ACS Energy Letters*, **7**, 1298-1307, (2022).

9 Lin, R. *et al.* All-perovskite tandem solar cells with improved grain surface passivation. *Nature* **603**, 73-78, (2022).
10 Brinkmann, K. O. *et al.* Perovskite-organic tandem solar cells with indium oxide interconnect. *Nature* **604**, 280-286, (2022).
11 Hörantner, M. T. *et al.* The Potential of Multijunction Perovskite Solar Cells. *ACS Energy Letters* **2**, 2506-2513, (2017).
12 Bai., Y. *et al.* Initializing film homogeneity to retard phase segregation for stable perovskite solar cells. *Science* **378**, 747-754, (2022).
13 Xu, j. Triple-halide wide-band gap perovskites with suppressed phase segregation for efficient tandems. *Science* **367**, 1097-1104, (2020).
14 Zhu, H. *et al.* Long-term operating stability in perovskite photovoltaics. *Nature Reviews Materials* **8**, 569-586, (2023).
15 Zhang, H. & Park, N.-G. Towards sustainability with self-healing and recyclable perovskite solar cells. *eScience* **2**, 567-572, (2022).
16 Zhang, H. *et al.* A universal co-solvent dilution strategy enables facile and cost-effective fabrication of perovskite photovoltaics. *Nat Commun* **13**, 89, (2022).
17 Podapangi, S. K. *et al.* Green solvents, materials, and lead-free semiconductors for sustainable fabrication of perovskite solar cells. *RSC Advances* **13**, 18165-18206, (2023).
18 Vidal, R. *et al.* Assessing health and environmental impacts of solvents for producing perovskite solar cells. *Nature Sustainability* **4**, 277-285, (2020).
19 Doolin, A. J. *et al.* Sustainable solvent selection for the manufacture of methylammonium lead triiodide ($MAPbI_3$) perovskite solar cells. *Green Chemistry* **23**, 2471-2486, (2021).
20 Küffner, J. *et al.* One-Step Blade Coating of Inverted Double-Cation Perovskite Solar Cells from a Green Precursor Solvent. *ACS Applied Energy Materials* **4**, 11700-11710, (2021).
21 Hang, P. *et al.* Highly Efficient and Stable Wide-Bandgap Perovskite Solar Cells via Strain Management. *Advanced Functional Materials* **33**, 2214381, (2023).
22 Abate, S. Y. *et al.* Eco-Friendly Solvent Engineered $CsPbI_{2.77}Br_{0.23}$ Ink for Large-Area and Scalable High Performance Perovskite Solar Cells. *Advanced Materials*, **36**, 2310279, (2024).
23 Yehao Deng, C. H. V. B., Xuezeng Dai, Jingjing Zhao, Bo Chen, Jinsong Huang. Tailoring solvent coordination for high-speed, room-temperature blading of perovskite photovoltaic films. *Science Advances* **5**, 7537, (2019).
24 Zuo, W. *et al.* Coordination Chemistry as a Universal Strategy for a Controlled Perovskite Crystallization. *Advanced Materials* **35**, 2302889, (2023).
25 Wang, J. *et al.* Highly Efficient Perovskite Solar Cells Using Non-Toxic Industry Compatible Solvent System. *Solar RRL* **1**, 1700091, (2017).
26 Yun, H.-S. *et al.* Ethanol-based green-solution processing of α-formamidinium lead triiodide perovskite layers. *Nature Energy* **7**, 828-834, (2022).
27 Park, N.-G. Green solvent for perovskite solar cell production. *Nature Sustainability* **4**, 192-193, (2020).
28 Wang, H. *et al.* Dimethyl sulfoxide: a promising solvent for inorganic $CsPbI_3$ perovskite. *Science Bulletin* **68**, 192-202, (2023).
29 Zheng, Y. *et al.* Blade Coating High-Quality Formamidinium-Cesium Lead Halide Perovskites with Green Solvent for Efficient and Stable Solar Cells. *Solar RRL* **6**, 2200737, (2022).
30 Jiang, Q. *et al.* Compositional texture engineering for highly stable wide-bandgap perovskite solar cells. *science* **378**, 1295-1300, (2022).
31 McMeekin, D. P. *et al.* Intermediate-phase engineering via dimethylammonium cation additive for stable perovskite solar cells. *Nature Materials* **22**, 73-83, (2022).
32 Huang, X., Cheng, F., Wu, B. & Zheng, N. Intermediate Chemistry of Halide Perovskites: Origin, Evolution, and Application. *The Journal of Physical Chemistry Letters* **13**, 1765-1776, (2022).
33 Li, H. *et al.* 2D/3D heterojunction engineering at the buried interface towards high-performance inverted methylammonium-free perovskite solar cells. *Nature Energy* **8**, 946-955, (2023).
34 Taylor, A. D. *et al.* A general approach to high-efficiency perovskite solar cells by any antisolvent. *Nature Communications* **12**, 1878, (2021).

35 Yang, Y. *et al.* Volatile Dual-Solvent Assisted Intermediate Phase Regulation for Anti-Solvent-Free Perovskite Photovoltaics. *Angewandte Chemie International Edition* **62**, 2300971, (2023).
36 Ahmadian-Yazdi, M.-R. & Eslamian, M. Effect of Marangoni Convection on the Perovskite Thin Liquid Film Deposition. *Langmuir* **37**, 2596-2606, (2021).
37 Braunger, S. *et al.* $Cs_xFA_{1-x}Pb(I_{1-y}Br_y)_3$ Perovskite Compositions: the Appearance of Wrinkled Morphology and its Impact on Solar Cell Performance. *The Journal of Physical Chemistry C* **122**, 17123-17135, (2018).
38 Zhang, F. *et al.* Vapor-Assisted In Situ Recrystallization for Efficient Tin-Based Perovskite Light-Emitting Diodes. *Advanced Materials* **34**, 2203180, (2022).
39 Guo, B. *et al.* In situ Stress Monitoring Reveals Tension and Wrinkling Evolutions during Halide Perovskite Film Formation. *ACS Energy Letters* **9**, 75-84, (2024).
40 Xu, F., Zhang, M., Li, Z., Yang, X. & Zhu, R. Challenges and Perspectives toward Future Wide-Bandgap Mixed-Halide Perovskite Photovoltaics. *Advanced Energy Materials* **13**, 2203911, (2023).
41 Zhu, C. *et al.* Strain engineering in perovskite solar cells and its impacts on carrier dynamics. *Nature Communications* **10**, 815, (2019).
42 Wang, H. *et al.* Interfacial Residual Stress Relaxation in Perovskite Solar Cells with Improved Stability. *Advanced Materials* **31**, 1904408, (2019).
43 Xue, D.-J. *et al.* Regulating strain in perovskite thin films through charge-transport layers. *Nature Communications* **11**, 1514, (2020).
44 Ruiz-Preciado, M. A. *et al.* Monolithic Two-Terminal Perovskite/CIS Tandem Solar Cells with Efficiency Approaching 25%. *ACS Energy Letters*, **7**, 2273-2281, (2022).
45 Wang, Z. *et al.* Suppressed phase segregation for triple-junction perovskite solar cells. *Nature* **618**, 74-79, (2023).
46 Wen, J. *et al.* Heterojunction formed via 3D-to-2D perovskite conversion for photostable wide-bandgap perovskite solar cells. *Nature Communications* **14**, 7118, (2023).
47 Cho, C. *et al.* Efficient vertical charge transport in polycrystalline halide perovskites revealed by four-dimensional tracking of charge carriers. *Nature Materials* **21**, 1388-1395, (2022).
48 Byeon, J. *et al.* Charge Transport Layer-Dependent Electronic Band Bending in Perovskite Solar Cells and Its Correlation to Light-Induced Device Degradation. *ACS Energy Letters* **5**, 2580-2589, (2020).
49 Qin, M., Chan, P. F. & Lu, X. A Systematic Review of Metal Halide Perovskite Crystallization and Film Formation Mechanism Unveiled by In Situ GIWAXS. *Advanced Materials* **33**, 2105290 (2021).
50 Zhang, H. *et al.* Pinhole-Free and Surface-Nanostructured NiO_x Film by Room-Temperature Solution Process for High-Performance Flexible Perovskite Solar Cells with Good Stability and Reproducibility. *ACS Nano* **10**, 1503-1511, (2016).